Ferromagnetic Superconductivity in Two-dimensional Niobium Diselenide

Tingyu Qu, Shangjian Jin, Fuchen Hou, Deyi Fu, Junye Huang, Darryl Foo Chuan Wei, Xiao Chang, Kenji Watanabe, Takashi Taniguchi, Junhao Lin, Shaffique Adam, Barbaros Özyilmaz*

* e-mail: barbaros@nus.edu.sg

Supplementary Information

Contents

1. Resistance-temperature superconducting transition curves

The resistance-temperature ($R - T$) superconducting transition curves are characterized by standard four-probe measurement. The $R - T$ curves of several representative junctions are shown in Fig. S1.1.

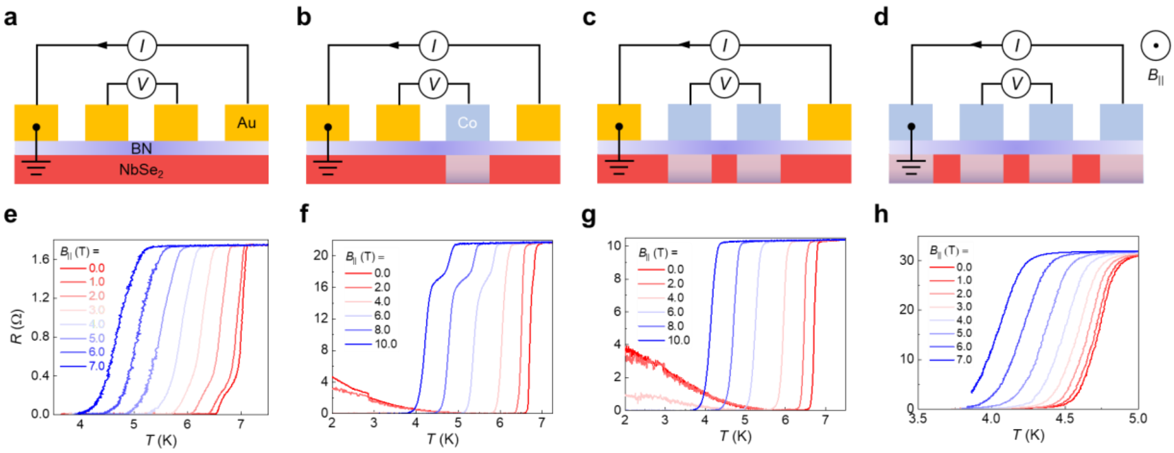

Fig. S1.1 | The $R - T$ curves of Devices A, C and E under discrete magnetic fields. a-d, Four-probe measurement configurations for E, A02, A01 and C, respectively. **e-h,** The $R - T$ curves of the corresponding junctions in **a-d** under discrete magnetic fields.

Based on the $R - T$ curves, we thus summarize the relation between $B_{C2||}$ and T_C of the four different junctions in Fig. S1.2. The magnetic doping concentration increases from Device E to A to C (Extended Data 10), where a prominent trend of Pauli limit violation can be seen.

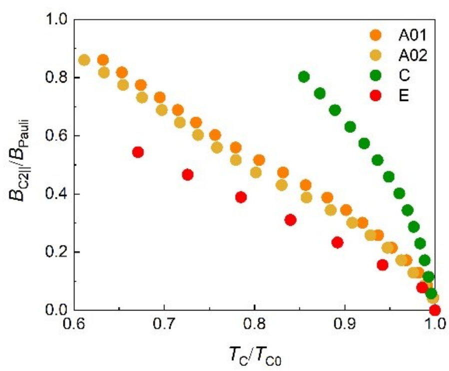

Fig. S1.2 | $B_{C2||}/B_{Pauli}$ vs. T_C/T_{C0} curves for the four junctions in Fig. S1.1.

2. Two-probe current-voltage measurement and differential conductance

First, we conduct two-probe measurement to characterize the current-voltage $(I - V)$ relation in Co/BN/$NbSe_2$/BN/Au junction, where the Co contact is connected to a DC-bias voltage source (generated by a Keithley-6300, Keithley Instruments) and the Au contact is grounded. The current tunnelling through the junction is simultaneously record by the Keithley-6300. The $I - V$ curve taken at $T = 2$ K and $B = 0$ is shown in Fig. S2.1.

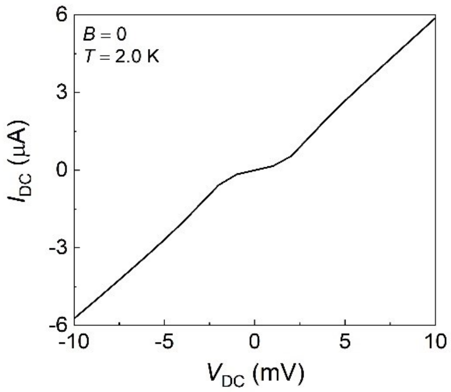

Fig. S2.1 | Two-probe $I - V$ curve for the tunnel junction.

Second, we conduct differential conductance (dI/dV) measurements to characterize the tunnelling spectrum of the superconducting $NbSe_2$. A small AC voltage (50 μV) is generated by a Lock-in Amplifier (SR830) and a DC-bias voltage is generated through a Keithley-6300. We sweep the DC-bias from –2 to +2 mV, and simultaneously record the AC current through the Lock-in Amplifier. The dI/dV is then calculated by the measured AC current divided by the constant AC voltage (50 μV). Figs. S2.2a and S2.2b show the temperature and magnetic field dependences of the dI/dV in 2D maps, respectively.

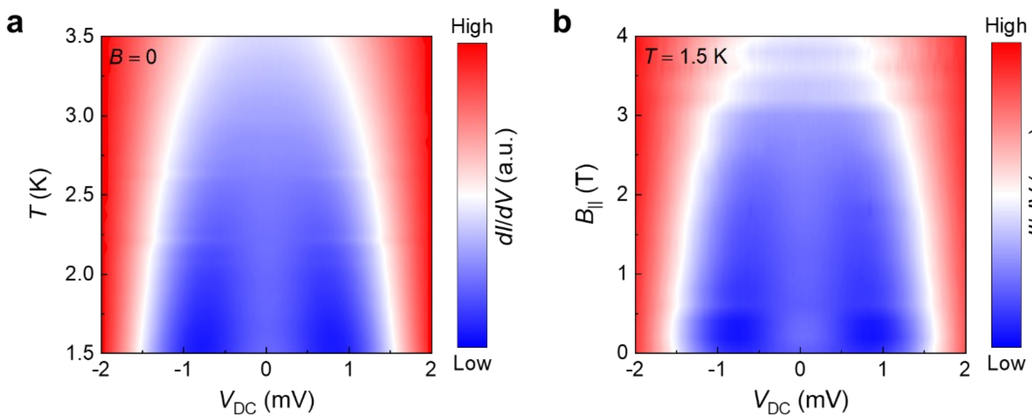

Fig. S2.2 | 2D maps of the dI/dV in the tunnel junction. a, Temperature dependence. **b,** Magnetic field dependence.

3. Analysis of superconducting gap symmetries and YSR states

The tunnelling spectrums show a prominent zero-bias peak (ZBP) in differential conductance (dI/dV) below a finite temperature and magnetic field. Our observation suggests localized in-gap bound states or Yu-Shiba-Rusinov (YSR) states in $NbSe_2$[1]. In addition, the superconducting gap is V-shaped below the superconducting transition temperature. To capture the symmetries of superconducting gap and the magnitude of YSR states, we analyse the differential conductance with a modified Bardeen–Cooper–Schrieffer (BCS) theory[2],[3] in the form of

$$\frac{dI}{dV}(V) = \frac{\sigma_N}{2\pi}\int_{-\infty}^{\infty} dE \left(\frac{df(\epsilon)}{d\epsilon}|_{\epsilon=E-eV}\right)\int_0^{2\pi} d\theta \, Re\left[\frac{E-i\Gamma}{\sqrt{(E-i\Gamma)^2-\Delta_0\cos^2(l\theta)}}\right] + \sigma_{\mathrm{ZBP}}\, exp\left(-\frac{V^2}{2\sigma^2}\right), \tag{1}$$

where the normal-state differential conductance σ_N is a constant from the measurement. The quasiparticle broadening Γ describe the broadening of the gap edge. The superconducting gap size $\Delta_0 \cos(l\theta)$ is angular-dependent with the orbital angular momentum quantum number l ($l = 0, 1, 2, 3$ for *s*-, *p*-, *d*-, and *f*-wave superconducting order parameters, respectively). For all nonzero angular momentum ($l \geq 1$), Equation (1) can be simplified to be the case of $l = 1$, thus we only consider $l = 0$ and 1 for singlet and triplet fittings. The second term describes the magnitude of YSR states.

An example of fitting the dI/dV by the *s*-wave and *p*-wave models is shown in Fig. S3a. We find that though both *s*-wave and *p*-wave models could fit the profile of dI/dV, the *p*-wave model implies a temperature or magnetic field threshold for the ZBPs closer to the T_{K} (~ 5 K) or B_{K} (3.5 T) for the resistance anomaly reflected by the four-probe $R-T$ measurement; while the *s*-wave model fails in fitting the shape of the tunnelling spectrum in many cases. This supports our claim that the resistance anomaly occurs due to a magnetic state induced by spin-triplet carriers inside the gap. Figs. S3b and S3c show the fitting results of the ZBP magnitude using the *p*-wave model, where the ZBP vanishes at the temperature or field close to T_{K} or B_{K}. In addition, our model predicts nearly the same superconducting gap size $\Delta_0 \approx 2.9$ meV at T_{K} and B_{K} points, suggesting that a sizeable superconducting gap plays a crucial role to harbour the localized magnetic states that trigger the resistive state below T_{K} or B_{K}.

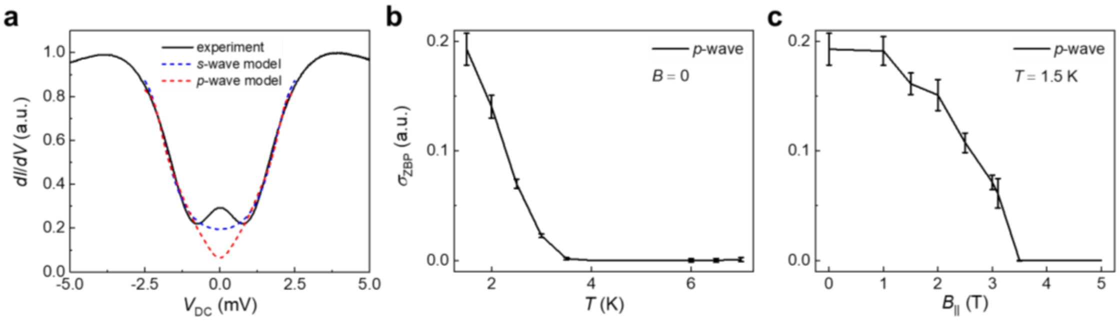

Fig. S3 | Analysis of ZBP by *s*-wave and *p*-wave models. a, Example of fitting the gap at $T = 1.5$ K and $B = 0$ with *s*-wave and *p*-wave models. **b,** Magnitude of ZBP (σ_{ZBP}) estimated by *p*-wave model as a function of temperature. **c**, Magnitude of ZBP (σ_{ZBP}) estimated by *p*-wave model as a function of magnetic field.

4. Switching mechanism in TMR

The negative switching in TMR can be understood by the two-current model[4] for parallel and anti-parallel alignment of Co contact and Co-$NbSe_2$ (Fig. S4). Under an external magnetic field that is along the easy axis of Co ($B_{||}$), both the spins of Co contact and Co impurities tend to align in the opposite direction to $B_{||}$. Importantly, the resistive state below T_C requires an anti-ferromagnetic (AFM) exchange coupling between Co impurities and itinerant spins from the Co-$NbSe_2$. This anti-ferromagnetic coupling would then encourage itinerant spins of Co-$NbSe_2$ to be parallel to $B_{||}$. Therefore, at low $B_{||}$, the AFM exchange is dominant and thus the itinerant spins in Co contact and Co-$NbSe_2$ are in anti-parallel configuration, thus leading to a high TMR. When the field is in-between the coercive fields of Co contact and Co-$NbSe_2$, a parallel configuration occurs, which gives rise to a low TMR. This is consistent with our observation that the TMR switches in the downward direction.

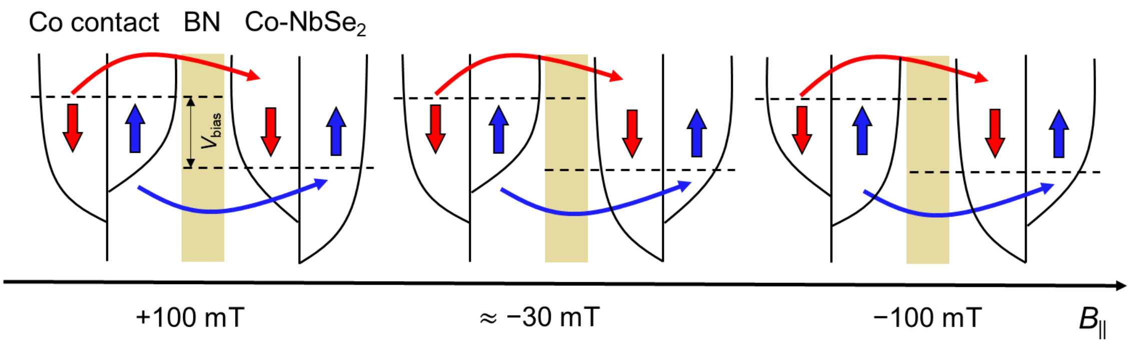

Fig. S4 | Schematics for the spin alignment between Co contact and itinerant spins of Co-$NbSe_2$.

5. Simulation of superconducting gap as a function of temperature and field

For simplicity, we calculate the superconducting gap using the s-wave Bardeen–Cooper–Schrieffer (BCS) theory. The superconducting gap $\Delta_{\mathrm{SC}}(T, B)$ is a function of temperature and magnetic field. The zero-temperature gap is estimated by the BCS relation $\Delta_{\mathrm{SC}}(0, B) = 1.76 k_B T_{\mathrm{C}}$, where the field dependent critical temperature T_{C} is taken from the measurement. Thus, temperature and field dependences of the gap are[5]

$$\ln\left[\frac{\Delta_{\mathrm{SC}}(T,B)}{\Delta_{\mathrm{SC}}(0,B)}\right] = -2\int_0^{\infty} dx \frac{1}{\sqrt{x^2 + \left(\frac{\Delta_{\mathrm{SC}}(T,B)}{k_B T}\right)^2}} \times \frac{1}{exp\sqrt{x^2 + \left(\frac{\Delta_{\mathrm{SC}}(T,B)}{k_B T}\right)^2} + 1}. \quad (2)$$

The simulation of superconducting gap is shown in Fig. S5. We find that the superconducting gaps show very close values at T_{K} and B_{K}. In addition, the relation between the Ginzburg–Landau coherence length at zero temperature and zero field ($\xi_{\mathrm{GL}}^0 = \xi_{\mathrm{GL}}(0,0)$) and the superconducting gap can be written by $\xi_{\mathrm{GL}}(0,0) = \hbar v_F / \pi\, \Delta_{\mathrm{SC}}(0,0)$, where $\hbar$ is the reduced Planck constant and v_F is the Fermi velocity. As the temperature or field increases, $\Delta_{\mathrm{SC}}(T, B)$ is reduced while ξ_{GL} becomes larger.

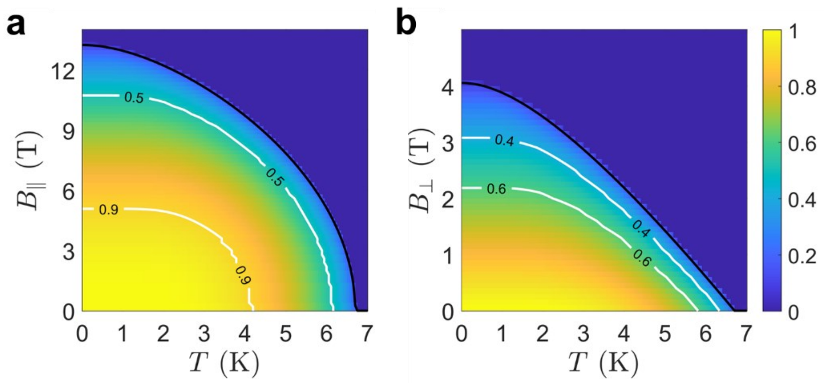

Fig. S5 | Simulation of the normalized superconducting gap size as a function of temperature and magnetic field ($\Delta_{\mathrm{SC}}(T,B)/\Delta_{\mathrm{SC}}(0,0)$). a, Under in-plane magnetic field. **b,** Under out-of-plane magnetic field.

6. RKKY interaction for the superconductivity-induced ferromagnetism

The Ruderman-Kittel-Kasuya-Yosida (RKKY) interaction refers to the indirect coupling between magnetic impurities through the conduction electrons[6]–[8]. In normal metal, the RKKY interaction decays with separation distance and oscillates with a period $(2k_F)^{-1}$, where k_F is the Fermi momentum. In *s*-wave superconductors, RKKY is predicted to be dominant when the separation distance is smaller than the superconducting coherence length ($r_i \leq \xi_{\mathrm{GL}}$)[9]. An enhanced antiferromagnetic exchange between impurities is predicted when the YSR states hybridize for distance $r_i < \xi_{\mathrm{GL}}$. However, in our Co-$NbSe_2$, the triplet-pairing state in $NbSe_2$ may create a ferromagnetic RKKY interaction[10]. Also, the recent study of RKKY interaction between the magnetic impurities in a spin-split superconductor[11] suggests the possibility of ferromagnetic exchange coupling. The Hamiltonian can be written as

$$H = H_{\mathrm{BCS}} - \sum_{\boldsymbol{k},\sigma} \sigma h_{ex} c_{\boldsymbol{k},\sigma}^{\dagger} c_{\boldsymbol{k},\sigma} + \sum_{\substack{\boldsymbol{k},\boldsymbol{k}' \\ \sigma,\sigma'}} \sum_{j} \frac{J}{N} e^{i(\boldsymbol{k}-\boldsymbol{k}')\cdot \boldsymbol{r}_j} \left(\boldsymbol{S}_j \cdot \boldsymbol{\sigma}_{\sigma\sigma'}\right) c_{\boldsymbol{k},\sigma}^{\dagger} c_{\boldsymbol{k}',\sigma'}, \tag{3}$$

where $H_{\mathrm{BCS}} = \sum_{\boldsymbol{k},\sigma} \epsilon_{\boldsymbol{k}} c_{\boldsymbol{k},\sigma}^{\dagger} c_{\boldsymbol{k},\sigma} + \sum_{\boldsymbol{k},\boldsymbol{k}'} V c_{\boldsymbol{k},\uparrow}^{\dagger} c_{-\boldsymbol{k},\downarrow}^{\dagger} c_{-\boldsymbol{k}',\downarrow} c_{\boldsymbol{k}',\uparrow}$ is the BCS Hamiltonian. In the second term, h_{ex} is the spin-split field induced by the external ferromagnet and is set to *z*-direction with $\sigma = \pm 1$. The third term is the *s*-*d* exchange Hamiltonian. J is the interaction between the impurity spins and itinerant spins and $\boldsymbol{\sigma}$ is the Pauli matrix. By considering the *s*-*d* exchange a perturbation term and compute the expectation value of the effective Hamiltonian numerically, the RKKY strength J_{RKKY} can be obtained. This formula concludes that below T_{C}, J_{RKKY} becomes ferromagnetic if the separation distance between the magnetic impurities is larger than the coherence length of the superconductor. In the case of a triplet superconductor, it is predicted that the induced ferromagnetism spreads over the scale of ξ_{GL}^{0}[11].

Supported by our experimental observation that both the ZBP and TMR switching disappears with temperature above T_{K}, we suggest that the ferromagnetic RKKY interaction between Co impurities requires a sizeable superconducting gap (equally, a short superconducting coherence length). In the following, we provide an intuitive calculation about how the relation between the superconducting coherence length and the magnetic impurity separation length determines the transition of RKKY below T_{C}.

We first estimate the average separation distance between the Co impurities. By the EELS characterization, in the topmost few layers of $NbSe_2$, the average Co concentration (through the penetration) is around 3%, and this can be rewritten in the form of

$$\frac{N_{\mathrm{Co}}}{N_{\mathrm{Co}}+N_{\mathrm{Nb}}+N_{\mathrm{Se}}} \cong 3\%, \tag{4}$$

which gives $\frac{N_{\mathrm{Co}}}{N_{\mathrm{Nb}}} \cong 0.09$. The lattice constant of $NbSe_2$ is $a = b = 3.489$ Å. Assuming the Co atoms are intercalated in the van der Waals gap of $NbSe_2$ evenly, the impurity separation distance within one unit cell can be estimated by

$$\frac{r_{\mathrm{Co}}^2}{a^2} = \frac{N_{\mathrm{Nb}}}{N_{\mathrm{Co}}} \tag{5}$$

Thus, we obtain r_{Co} around 1.2 nm.

We then estimate the superconducting coherence lengths. ξ_{GL}^0 is extracted by fitting the experimental $B_{\mathrm{C2||}} - T_{\mathrm{C}}$ curve using the pair-breaking equation shown in Methods, where we find $\xi_{\mathrm{GL}}^0 \approx 5.7 \pm 1.2$ nm in Device A. Below 4 K ($T_{\mathrm{C0}} = 6.60$ K), we observe a resistive phase and ferromagnetism in this device. The exchange interaction between magnetic impurities in the superconducting host can be dominated by RKKY interaction if $\gamma \cdot r_{\mathrm{Co}} > \xi_{\mathrm{GL}}$, where γ is a constant. In the heavily doped devices, we do not observe clear signatures of spin flips below T_{C}. Possibly, r_{Co} becomes far smaller than ξ_{GL}, thus the RKKY interaction falls into a regime where the ferromagnetic order and anti-ferromagnetic order alternate, and a net ferromagnetism is not observable. We thus summarize the phenomenological picture in Fig. S6 to demonstrate the origin of the superconductivity-mediated ferromagnetism.

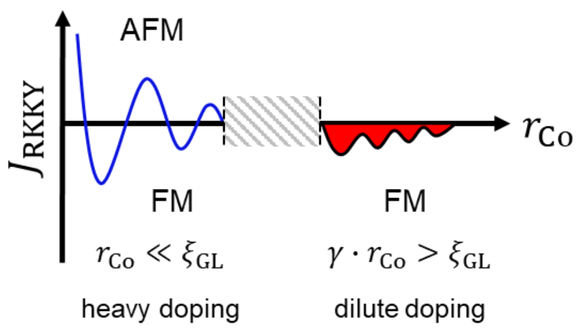

Fig. S6 | Schematics of RKKY interaction in a superconducting host with different magnetic doping levels. In the heavy doping case, the ferromagnetic order (FM) and anti-ferromagnetic order (AFM) alternate and the RKKY coupling strength (J_{RKKY}) peaks with an AFM order. In the dilute doping case, a net FM RKKY could occur with a sufficiently large spin-split field. The shadowed region refers to a transition regime.

7. The interaction between ferromagnetism and triplet pairing

Here, we interpret that in our Co-$NbSe_2$, how the RKKY-mediated ferromagnetism co-exists with the Cooper pairs and the possible origin of the resistive state below T_{K}.

The coexistence of ferromagnetism and superconductivity have been suggested in several heavy fermions[12]–[16], and all of these materials favour a spin-triplet superconducting order parameter.

In general, the SC gap function can be written as $\Delta^{\boldsymbol{k}} = i\sigma_y\left(d_{\boldsymbol{k}0} I_{2\times 2} + \vec{d}_{\boldsymbol{k}} \cdot \vec{\sigma}\right)$, where $\vec{\sigma}$ is the Pauli matrix[17],[18]. The singlet and triplet order parameters, $d_{\boldsymbol{k}0}$ and $\vec{d}_{\boldsymbol{k}}$ are governed by the symmetry properties of the fermion pair interaction with respect to their momentum $\boldsymbol{k}$. An inversion symmetric interaction $V_{\boldsymbol{k}}^S = V_{-\boldsymbol{k}}^S$ results in $\vec{d}_{\boldsymbol{k}} = 0$; while an inversion antisymmetric interaction $V_{\boldsymbol{k}}^A = -V_{-\boldsymbol{k}}^A$ results in $d_{\boldsymbol{k}0} = 0$. A pairing mixing of spin singlet and triplet occurs at $V_{\boldsymbol{k}} = V_{\boldsymbol{k}}^S + V_{\boldsymbol{k}}^A$. In our case, the RKKY-mediated ferromagnetism breaks the reversal symmetry, and further supports spin-triplet components[17],[18]. This means that the ferromagnetic Co-$NbSe_2$ could generate excess triplets and gives rise to a high spin injection efficiency to the superconducting $NbSe_2$ channel.

Then we interpret the possible origin of the resistance anomaly. As the temperature decreases below T_{K}, the emergence of ferromagnetic order does not destroy the superconductivity given the evidence of the re-entrant superconductivity in our experiment, which is also consistent with the RKKY-triggered resistive state below T_{C} in $Eu(Fe0.89Co0.11)_2As_2$[19]. In our case, the resistance anomaly could result from the spin-flipping scattering between the magnetization in Co atoms and the spin-triplet Cooper pairs[20],[21]. As the magnetic field increases, the RKKY interaction is weakened due to the increased superconducting coherence length and finally disappears at B_{K}. The high field suppresses the ferromagnetism and leads to a re-entrant superconducting phase.

8. NLSV signals at different temperatures

To address the role of superconductivity on the spin-flip signals in NLSV measurement, we show non-local resistance (R_{NL}) as a function of in-plane magnetic field ($B_{\parallel}$) for two different Co/BN/$NbSe_2$ spin valves measured above and below T_{C0}.

Device No.	T_{C0}	Temperature condition for the switch in NLSV
Device A01	6.60 K	Presence of switch in NLSV measurement at 1.5 K Absence of switch in NLSV measurement at 7.0 K
Device B	3.50 K	Presence of switch in NLSV measurement at 53 mK Absence of switch in NLSV measurement at 4.0 K

The $R - T$ curves of the two devices are shown in Figs. S8a and S8b and the $R_{\mathrm{NL}} - B_{\parallel}$ curves of the two devices are shown in Figs. S8c and S8d.

In Device A and Device B, we observe spin-flip signals in NLSV at 1.5 K and 50 mK, respectively; however, we do not observe any switch in NLSV measurement above T_{C0} in either Device A or Device B.

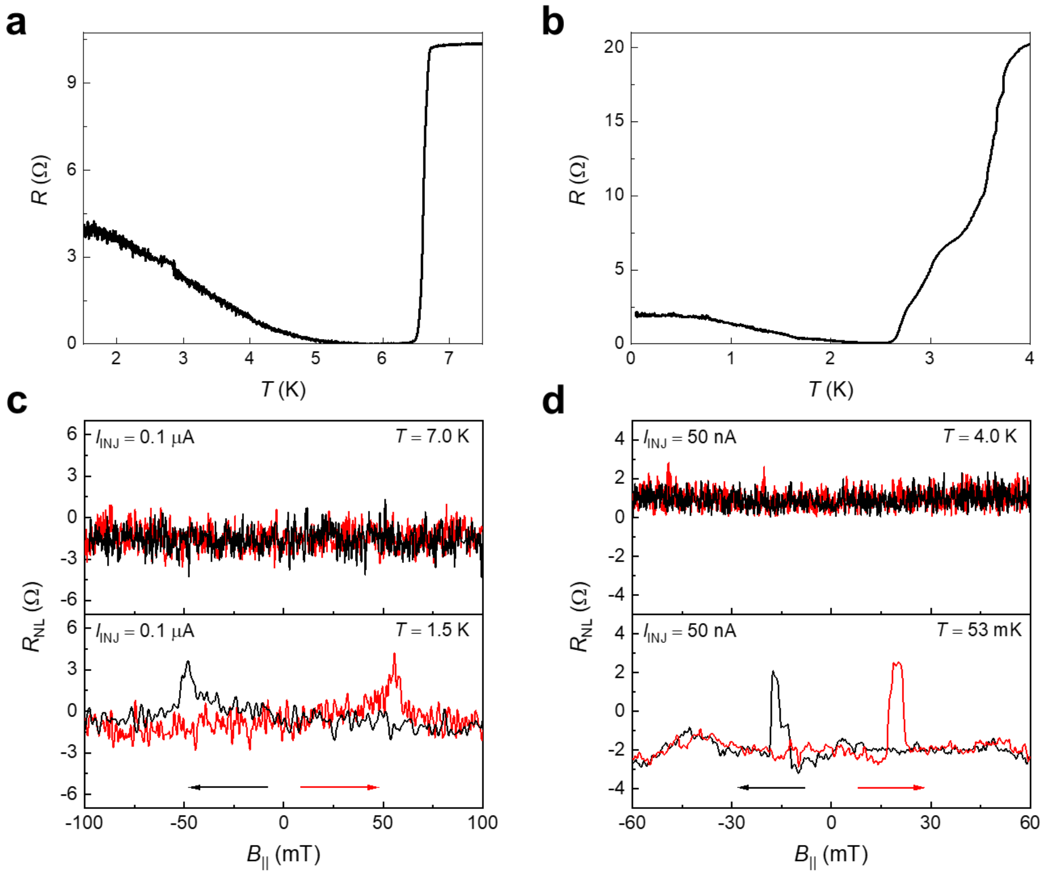

Fig. S8 | NLSV signals at different temperatures. **a**, Zero-field $R - T$ curve of Device A. **b**, Zero-field $R - T$ curve of Device B. **c**, R_{NL} vs. $B_{||}$ at $T > T_{\mathrm{C0}}$ and $T < T_{\mathrm{C0}}$ for Device A. **d**, R_{NL} vs. $B_{||}$ at $T > T_{\mathrm{C0}}$ and $T < T_{\mathrm{C0}}$ for Device B.

9. TMR and NLSV signals with different BN thicknesses

The residual resistance ratio (RRR) is an indicator of the Co doping level in $NbSe_2$ and is defined by $RRR = R_{273K}/R_{T_C^+}$, where $R_{T_C^+}$ refers to the resistance just above T_C. To address the role of Co doping for the observed ferromagnetism and spin injection in $NbSe_2$, we compare two devices with different BN thicknesses.

Device No.	Layers of BN	T_{C0}	RRR	Spin signal from TMR and NLSV
Device A01	3	6.60 K	7.6	Yes
Device D	5	6.80 K	9.0	No

The $R-T$ curves of the two devices are shown in Figs. S9a and S9b and the $TMR-B_{\parallel}$ curves of the two devices are shown in Figs. S9c and S9d.

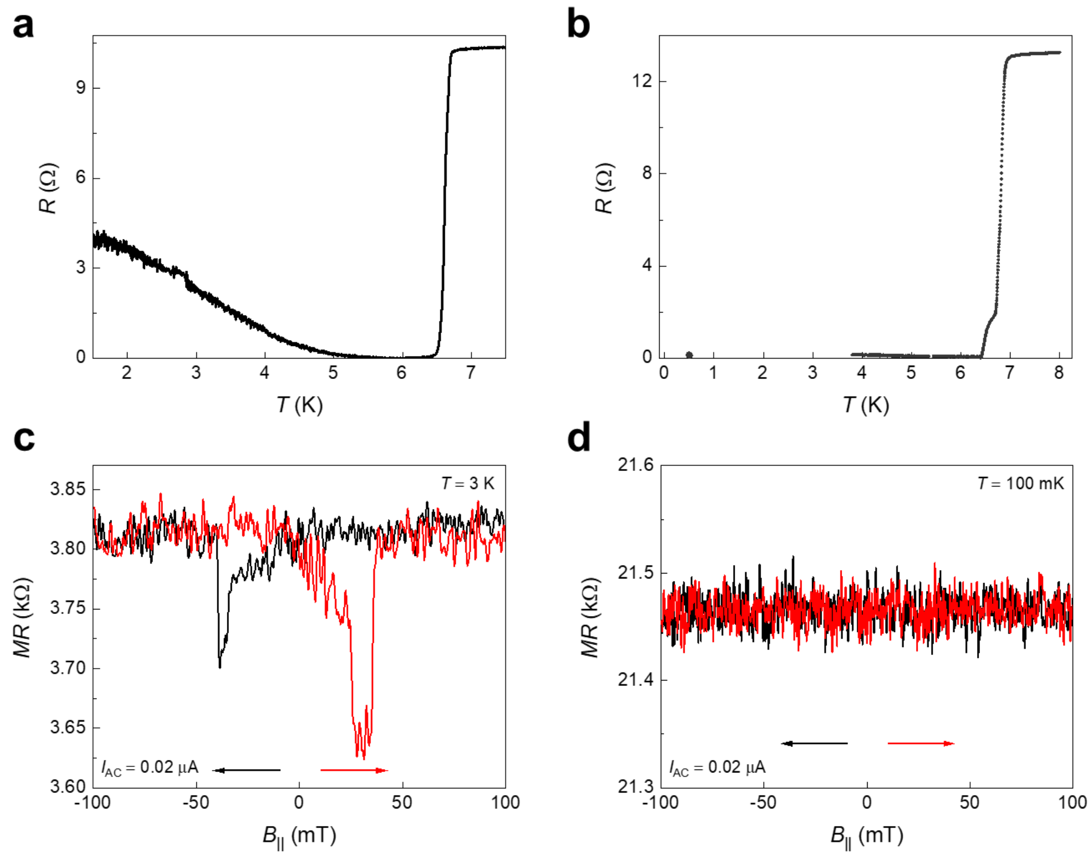

Fig. S9 | TMR signals in Device A and Device D. **a**, Zero-field $R-T$ curve of Device A. **b**, Zero-field $R-T$ curve of Device D. **c**, MR vs. $B_{||}$ at $T = 3$ K for Device A. **d**, MR vs. $B_{||}$ at $T = 100$ mK for Device D.

10. Analysis of Hanle precession in superconducting channels

To show that the non-local signal does not result from any local tunnelling effect, we simultaneously record the local resistance (R_{L}) and non-local resistance (R_{NL}), as shown in the top and bottom panels in Fig. S10, respectively. None of the local signals shows convergence or oscillation as a function of magnetic field, while the non-local signals clearly show a convergence at large field or even a second peak at intermediate field, in agreement with the picture of the precession of diffused spins.

Then we present our analysis of the Hanle precession. The phenomenological model has been established by Jedema, F. J., et al[22] to understand the non-local resistance in the metallic state, which consists of a diffusion distribution function, a spin relaxation and a spin precession term,

$$R_{\mathrm{NL}}^{0} = R_0 \int_0^{\infty} dt \frac{1}{\sqrt{4\pi D t}} e^{-\frac{{L_{\mathrm{CH}}}^2}{4Dt}} e^{-\frac{t}{\tau}} \cos(\omega_{\mathrm{L}} t), \tag{6}$$

with a scale factor R_0 for the resistance, the spin diffusion constant D, the spin transport channel length L_{CH}, the spin relaxation time τ, and the Larmor frequency $\omega_L = g\mu_B B_{\perp}/\hbar$. The calculated R_{NL}^{0} can well fit the Hanle precession data for L_{CH} = 0.6 and 0.8 μm, where we extract spin relaxation lengths $\lambda_s = \sqrt{D\tau} \sim 0.62$ and 1.06 μm, respectively (Fig. 4d in the main text). However, this model is unable to describe the second peak in R_{NL} (without a sign change) for L_{CH} = 3.0 μm (see Fig. S10c). Notably, $NbSe_2$ is a Type-II superconductor with $B_{\mathrm{C1}} \approx 20$ mT[23], thus the field screening effect by the vortices should play a role for the spin precession. In fact, we observed a zero-field dip in R_{NL} occurring at the field range of 10~20 mT in all the three channels, consistent with the B_{C1} of $NbSe_2$, which indicates that Meissner effect indeed occurs in the superconducting channel.

We thus modify the standard Hanle model by introducing the vortices as an additional dephasing factor in the superconducting channel,

$$R_{\mathrm{NL}} = R_0 \int_0^{\infty} dt \frac{1}{\sqrt{4\pi D t}} e^{-\frac{L^2}{4Dt}} e^{-\frac{t}{\tau}} [1 - a_v + a_v \cos(\omega_L t)], \tag{7}$$

where $a_v = 1 - \exp(-B/B_v)$ is used to count the proportion of the vortex area and B_v represents the magnetic field that is responsible for the vortices. By making this modification, the spin transport in the superconducting channel is separated into a precession regime with proportion a_v and a non-vortex regime with proportion $(1 - a_v)$.

Our modified Hanle model could well fit $L_{\mathrm{CH}} = 0.8$ μm, providing $D \approx 0.004$ m^2·s^{-1} and $\tau \sim$ 235 ps that are close to the values extracted by the standard Hanle model. For $L_{\mathrm{CH}} = 3.0$ μm, the modified Hanle model could capture the second peak in R_{NL} without a sign change. However, we notice that the extracted $\lambda_{\mathrm{s}} = \sqrt{D\tau} \sim 0.22$ µm is not comparable to that for $L_{\mathrm{CH}} =$ 0.6 and 0.8 µm ($\lambda_{\mathrm{s}} > 0.6$ µm). We provide two possible reasons. First, our modified Hanle model could not fit the curvature of R_{NL} in the small field range, which underestimates the relaxation. Further investigation is needed for a more plausible Hanle model in a superconducting channel. Second, it is noted that though our channel mainly consists of the undoped $NbSe_2$, the Co-$NbSe_2$ may play a role on spin scattering. Therefore, the average spin relaxation time (τ) of the whole channel should be estimated by $\tau^{-1}(L_1 + L_2) = \tau_1^{-1}L_1 + \tau_2^{-1}L_2$, where L_1 and L_2 are the lengths of $NbSe_2$ and Co-$NbSe_2$, respectively. The overall spin relaxation can be limited by the scattering from Co-$NbSe_2$. However, both the standard and our modified Hanle models suggest rather long triplet diffusion (up to micrometre) in the superconducting $NbSe_2$, which provides strong evidence for the presence of an intrinsic spin-triplet pairing state in $NbSe_2$.

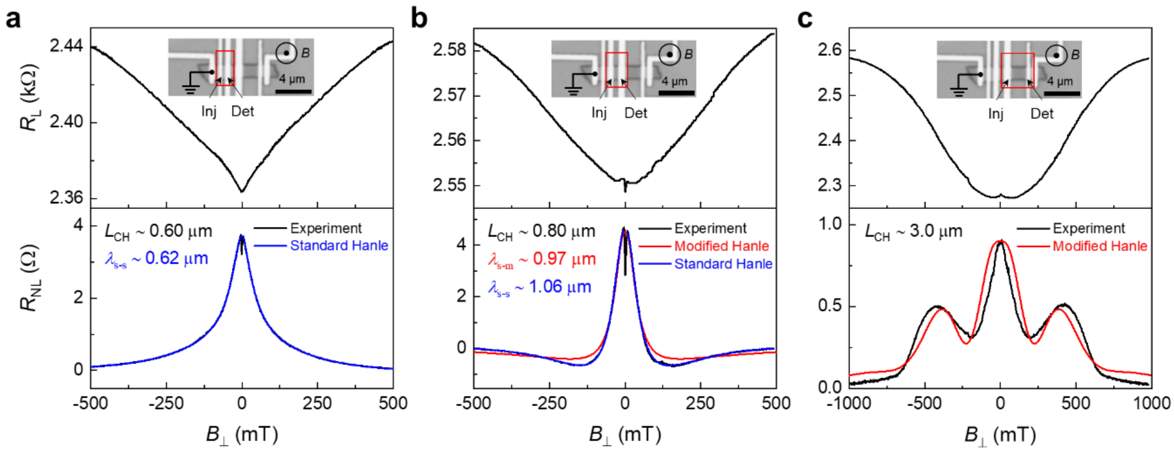

Fig. S10 | Analyses of Hanle precession curves in the superconducting regime. Top figures and bottom figures in **a**–**c** represent the local and non-local signals, respectively. L_{CH} = 0.6, 0.8, and 3.0 µm, respectively, in **a**–**c**. The red curves present the fitting of the Hanle precession curves, where the standard Hanle model is applied in **a** and **b**; and the modified Hanle model is applied in **b** and **c**. $\lambda_{\mathrm{s-m}}$ and $\lambda_{\mathrm{s-s}}$ refer to spin diffusion lengths extracted by the modified and standard Hanle models, respectively. Insets: Optical micrographs of the measured superconducting spin valve junctions.

11. References

[1] Sticlet, D., & Morari, C. Topological superconductivity from magnetic impurities on monolayer NbSe2. *Phys. Rev. B* **100**, 075420 (2019).

[2] Dynes, R. C., Narayanamurti, V., & Garno, J. P. Direct measurement of quasiparticle-lifetime broadening in a strong-coupled superconductor. *Phys. Rev. Lett.* **41**, 1509 (1978).

[3] Oh, M., *et al*. Evidence for unconventional superconductivity in twisted bilayer graphene. *Nature* **600**, 240–245 (2021).

[4] Fert, A., & Campbell, I. A. Two-current conduction in nickel. *Phys. Rev. Lett.* **21**, 1190 (1968).

[5] Tinkham, M. Introduction to superconductivity. Courier Corporation (2004).

[6] Ruderman, M. A., & Kittel, C. Indirect exchange coupling of nuclear magnetic moments by conduction electrons. *Phys. Rev.* **96**, 99 (1954).

[7] Kasuya, T. A theory of metallic ferro-and antiferromagnetism on Zener's model. *Prog. Theor. Phys.* **16**, 45–57 (1956).

[8] Yosida, K. Magnetic properties of Cu-Mn alloys. *Phys. Rev.* **106**, 893 (1957).

[9] Yao, N. Y., Glazman, L. I., Demler, E. A., Lukin, M. D., & Sau, J. D. Enhanced antiferromagnetic exchange between magnetic impurities in a superconducting host. *Phys. Rev. Lett.* **113**, 087202 (2014).

[10] Schmid, H., Steiner, J. F., Franke, K. J., & von Oppen, F. Quantum Yu-Shiba-Rusinov dimers. *Phys. Rev. B* **105**, 235406 (2022).

[11] Ghanbari, A., & Linder, J. RKKY interaction in a spin-split superconductor. *Phys. Rev. B* **104**, 094527 (2021).

[12] Saxena, S. S., *et al*. Superconductivity on the border of itinerant-electron ferromagnetism in UGe2. *Nature* **406**, 587–592 (2000).

[13] Aoki, D., *et al*. Coexistence of superconductivity and ferromagnetism in URhGe. *Nature* **413**, 613–616 (2001).

[14] Pfleiderer, C., *et al*. Coexistence of superconductivity and ferromagnetism in the d-band metal ZrZn2. *Nature* **412**, 58–61 (2001).

[15] Ran, S., *et al*. Nearly ferromagnetic spin-triplet superconductivity. *Science* **365**, 684–687 (2019).

[16] Jiao, L., *et al*. Chiral superconductivity in heavy-fermion metal UTe2. *Nature* **579**, 523–527 (2020).

[17] Sigrist, M., & Ueda, K. Phenomenological theory of unconventional superconductivity. *Rev. Mod. Phys.* **63**, 239 (1991).

[18] Smidman, M., Salamon, M. B., Yuan, H. Q., & Agterberg, D. F. Superconductivity and spin–orbit coupling in non-centrosymmetric materials: a review. *Rep. Prog. Phys.* **80**, 036501 (2017).

[19] Jiang, S., *et. al*. Superconductivity and local-moment magnetism in Eu(Fe 0.89Co0.11)2As2. *Phys. Rev. B* **80**, 184514 (2009).

[20] Felsch, W., & Winzer, K. Magnetoresistivity of (La, Ce) Al2 alloys. *Solid State Commun.* **13**, 569–573 (1973).

[21] Kochan, D., Barth, M., Costa, A., Richter, K., & Fabian, J. Spin relaxation in s-wave superconductors in the presence of resonant spin-flip scatterers. *Phys. Rev. Lett.* **125**, 087001 (2020).

[22] Jedema, F. J., Heersche, H. B., Filip, A. T., Baselmans, J. J. A., & Van Wees, B. J. Electrical detection of spin precession in a metallic mesoscopic spin valve. *Nature* **416**, 713–716 (2002).

[23] Boaknin, E., *et al*. Heat Conduction in the Vortex State of NbSe2: Evidence for Multiband Superconductivity. *Phys. Rev. Lett.* **90**, 117003 (2003).